Wafer-scale strain engineering on silicon for fabrication of ultimately controlled nanostructures

Hiroo Omi,* David J. Bottomley,† Yoshikazu Homma, and Toshio Ogino‡

NTT Basic Research Laboratories, NTT Corporation, 3-1 Wakamiya, Morinosato, Atsugi, Kanagawa 243-0198, Japan

(Received 15 May 2002; revised manuscript received 4 September 2002; published 3 March 2003)

We propose a method of strain distribution control on planar Si(001) and Si(111) wafers for nanostructure self-assembly, taking a long-term view toward future Si semiconductor science and technology. Oxygen ions are implanted through patterned layers on the Si wafers. The sample is then annealed at 1325 °C to produce bulk oxide inclusions that yield a tensile and/or compressive strain distribution on the silicon surface. We also demonstrate that strained epitaxial growth of Ge on the Si(001) substrate surface at 550 °C in an ultrahigh vacuum produces three-dimensional islands whose location and size distribution are well controlled. The degree of localization control is in agreement with simulations of the elastic strain distribution. Additionally, we show that increasing the Ge growth temperature 50 °C significantly reduces the density of stray dots that randomly grow on the Si surface. The samples were observed by atomic force microscopy and cross-sectional transmission electron microscopy. Strains on the silicon surface, produced by the buried silicon oxides, were measured by micro-Raman spectroscopy.

DOI: 10.1103/PhysRevB.67.115302 PACS number(s): 81.07.Ta, 68.55.−a

I. INTRODUCTION

The mainstay of Si technology is high-density integration of submicron scale devices on a large-diameter wafer.[1] The ultimate goal is wafer-scale fabrication of atomically controlled nanostructures. As the Si wafer diameter increases and device sizes decrease, however, the number of patterns that must be formed on the Si wafer surface increases rapidly. Although scanning probe techniques have achieved atomic scale patterns,[2] such techniques cannot be applied to economical high-density integration due to their unfeasibly low serial throughput. Recently, nanofabrication and pattern formation, based on a surface phenomenon called self-assembly or self-organization, have attracted much[3] attention because of the potential impact these will have on the next generation of Si technology. For example, quantum dots[4–6] and quantum wires[7] are self-assembled without lithographic techniques in lattice-mismatched epitaxial systems such as Ge on Si. The advantages of these processes are high throughput and much smaller dimensions than the lithographic limit. On the other hand, the wafer-scale control required in Si integration is difficult to achieve by only self-assembly because self-assembly can guarantee only a local ordering. These technological considerations naturally lead us to conclude that atomically well controlled surface structures on the silicon wafer scale have good potential as templates for nanostructure fabrication based on self-assembly.

In most research to date on nanostructure formation on Si surfaces, however, the substrate has not been subjected to advanced preparation procedures. Preparation has typically consisted of chemical etching followed by thermal treatment in an ultrahigh vacuum. Without localization control, the size variation of Ge or Ge_xSi_{1-x} alloy nanostructures grown coherently on the surface is appreciable. As a result, the structures are not suitable for commercial applications.[4–7] A recent exception with regard to the size variation is the work of Schmidt *et al.*, in which electron beam lithography was used to create a pattern that enabled the growth of evenly spaced Ge nanostructures with a narrow size distribution.[8] Electron beam lithography suffers from a throughput scaling problem, however: wafer throughput decreases as device sizes decrease because the pattern writing time increases. In other notable recent work, the growth of Ge islands on Si mesa structures led to ordered island ("dot") patterns.[9,10] However, a planar wafer surface is desired by industry because mesa patterns limit the device structures and fabrication processes that can be employed.

It is well known that elastic strain or stress is one of the significant factors governing physical and chemical processes on a surface, and that it might be useful in nanotechnology fabrication on silicon wafers. For example, Teichert *et al.* reported that periodic arrays of uniform SiGe islands were obtained by the modulation of surface strain in epitaxial Si layers in molecular-beam epitaxy. The strain in the Si film was due to buried SiGe islands in SiGe/Si multilayers.[3,11,12] If the designed strain distribution on a Si planar surface could be achieved on the nanoscale, as reported by Teichert *et al.*, it would be a good candidate for nanostructure fabrication on the wafer scale. Despite the significance and potential of designed patterns of strain and stress distributions on wafer surfaces, however, no methods for preparing them have been proposed. Also, little attention has been paid to strain distribution control for nanostructure fabrication directly on the silicon wafer scale.

Against this background, we proposed a commercially viable industrially proven process to prepare Si wafers for advanced nanostructure fabrication. We have already proposed a method of strain-distribution control on Si(001) wafers, and demonstrated that the strain-distribution-controlled substrate succeeds in controlling the localization and size of Ge islands in self-assembly and the shape of atomic steps on Si(111).[13,14] This paper is a detailed report on our progress, including the results on Si(001) and Si(111) wafers. Section II describes our key idea to achieve our goal and gives experimental details. Section III A presents the typical results of strain distribution control on Si(001) and Si(111). Section III B describes Ge island self-assembly on strain-distribution-controlled Si(001) substrates and discusses the

 ©2003 The American Physical Society

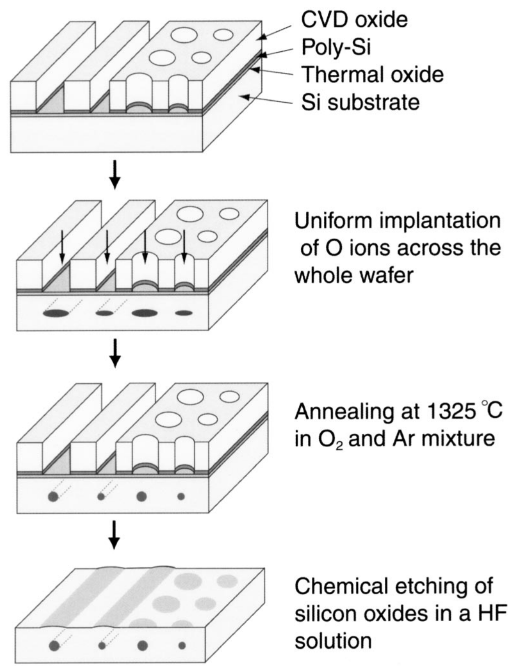

FIG. 1. Schematic diagram of the process for producing strain distribution controlled Si substrates with line and hole patterns.

localization of Ge island growth using linear isotropic elasticity theory. Section IV concludes the paper.

II. KEY IDEA AND EXPERIMENTS

As shown schematically in Fig. 1, oxide inclusions are formed at selected places within the Si bulk by implanting O ions through a poly-Si and SiO_2 mask. The mask consists of an 800-nm-thick chemical vapor deposition (CVD) oxide on top of 100 nm of poly-Si which lies on top of a 100-nm-thick thermal oxide, which is in turn on top of the Si wafer. The polycrystalline Si layer acts as an etch stop for the CVD oxide mask. The ion implantation is done at an energy of 180 keV and a substrate temperature of 450 °C. Openings for implantation are created by optical lithography, which leaves behind only the thermal oxide layer. The substrate and its pattern are annealed in an Ar atmosphere containing $0.20 \pm 0.01\%$ O_2 at 1325 ± 5 °C for 2.5 h, and finally the pattern is removed by a lift-off etch in a $HF:H_2O$ 1:3 solution. The volume of the oxide inclusions formed during the annealing is approximately double their Si content prior to implantation. The stress produced by the inclusions leads to a strain distribution at the Si wafer surface as described in the related theoretical work by Tersoff, Teichert, and Lagally.[12] We use this strain distribution for nanofabrication and nanostructure positional control. Note that the oxide inclusions are completely stable up to at least 1325 °C and are therefore compatible with any subsequent fabrication process in standard Si technology.

The approach combining O ion implantation and annealing is a spinoff from the silicon on insulator (SOI) field, specifically the separation by implanted oxygen (SIMOX) process invented 24 years ago at NTT.[15] The SOI technology field was recently reviewed by Colinge and Bower.[16] Enormous improvements in the SOI silicon layer have been achieved over the past 20 years of research and development, principally at industrial laboratories such as our own. SOI is playing an increasingly important role in low-voltage low-power circuitry,[17] and SOI knowhow has contributed to the different process reported here.

In order to demonstrate the process in Fig. 1 on the wafer scale, six six-inch-diameter Si wafers, four (001) and two (111) in orientation, were used. The Si(001) wafers were miscut by 0.5° towards the [100] direction. Following surface layer deposition and optical lithography, the four (001) orientation wafers were implanted with O ions at densities of 2×10^{17}, 5×10^{16}, 3×10^{16}, and 1×10^{16} cm^{-2}, and the two (111) wafers were implanted at densities of 2×10^{17} and 5×10^{16} cm^{-2}. We hereafter refer to 2×10^{17} cm^{-2} as high-density implantation and 5×10^{16} cm^{-2} as low-density implantation. The O ion implantation energy was 180 keV. Implantation was uniform across the whole wafer; the ions were stopped by the CVD oxide in places so covered. The wafers were then cleaved into square pieces 15 mm to a side. The pieces were employed in chemical etching and annealing experiments to determine suitable processes for producing strain distribution controlled substrates.

A conventional molecular-beam epitaxy (MBE) chamber was used to grow Si and Ge on the strain distribution controlled Si(001) substrate. The substrate surface was cleaned in the MBE chamber. Si deposition was done using an electron-beam evaporator at a substrate temperature of 600 ± 20 °C. Ge depositions were done using a Knudsen cell at substrate temperatures of 550 ± 20 and 600 ± 20 °C. 200-nm-thick Si buffer layers were grown only on the high-density Si(001) sample for the Raman measurement. Ge coverages were below 9 monolayers (ML's), where 1 ML $=6.3\times10^{14}$ atoms cm^{-2}. The deposition rate was 0.09 nm min^{-1}. The pressure during the Ge deposition was 5×10^{-10} Torr.

Surface morphology was observed by tapping-mode atomic force microscopy (AFM) in air. Cross-sectional transmission electron microscopy (XTEM) images were obtained using the transmission, {200} and {111} beams, performed at 300 keV. The point resolution was 0.18 nm.

Raman spectra were taken in a backscattering geometry at room temperature using the 457.9-nm wavelength line of an argon ion laser as a light source. The power and diameter of the focused laser beam were 5 mW and 1 μm, respectively. Incident light was polarized in the scattering plane, while scattered light was collected without polarization analysis. The spectra were analyzed with a Ramanor U-1000 (Jobin Yvon) micro-Raman system.

III. RESULTS AND DISCUSSIONS

A. Strain distribution control on Si(001) and Si(111)

Figure 2 shows cross-sectional TEM images obtained from the high- and low-density O implanted samples before and after annealing at 1325 °C. As seen in Fig. 2(a), most of the oxygen ions were implanted to a depth of 200–500 nm at the center of the mask opening. Some oxygen ions, however, stopped near the edge of the opening, which may be due to a

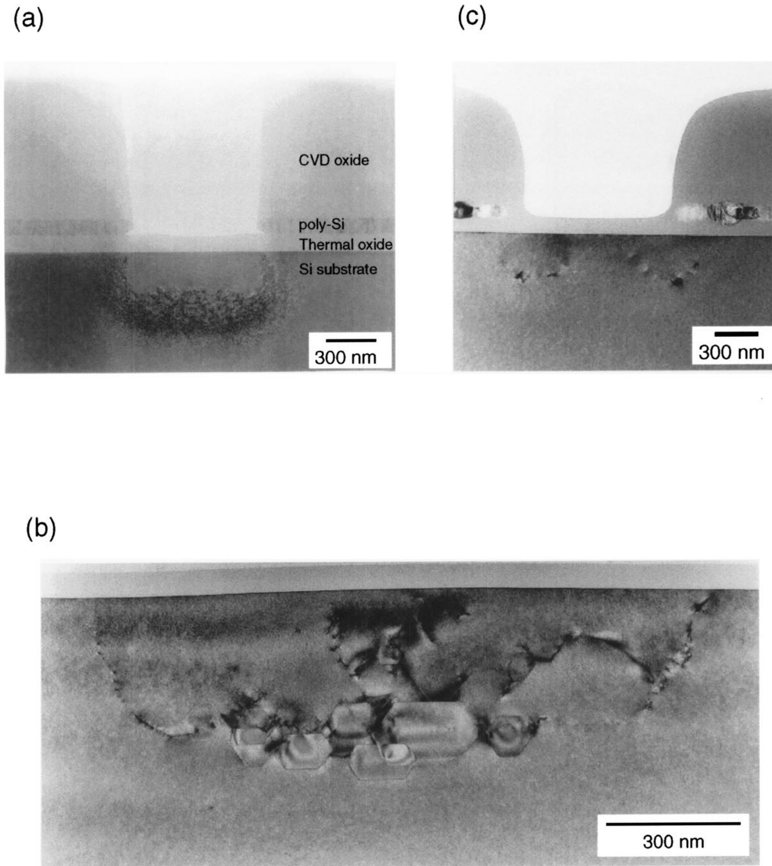

FIG. 2. Cross-sectional TEM images of line patterns on Si. (a) 700-nm-wide line pattern on Si(111) perpendicular to the $(11\bar{2})$ image plane, before annealing. (b) 700-nm-wide line pattern perpendicular to the (110) image plane on Si(001) after annealing to 1325 °C for the high-implantation-density sample. (c) is same as (b), except that the sample is the low-implantation-density one.

mask edge effect. For the high-density implantation Si(001) sample, the annealing produced oxide inclusions in the bulk [Fig. 2(b)]. The inclusions are facetted and are about 100 nm wide, 150 nm high, and are at a depth of about 300 nm. The distance between them is about 100 nm. Numerous line defects around the inclusions due to excessive stress are observed, but in the low-density case no line defects reach the surface. The low-density substrate quality is sufficient for our purposes for growing Ge nanostructures on a silicon wafer scale, as described in the next section. For the low-density sample, although the presence of the inclusions is clear from AFM, which shows that the surface has risen about 1–2 nm in the implanted regions as described later, no inclusions are visible in the cross-sectional TEM image [Fig. 2(c)]. This is because they are too small to observe by TEM. Therefore for later theoretical purposes we treat a silicon oxide inclusion as a point inclusion in this case and the distances between these inclusions are assumed to be the same as in the 2×10^{17} cm^{-2} implantation case.

In the XTEM images of Si(111) samples after annealing at 1325 °C, we see that the line defects due to the silicon oxide inclusions reached the surface in the high-density implantation sample, but no defects are visible around the oxide inclusions in the low-density implantation sample.

For wafers prepared differently than shown in Fig. 1, namely by etching off the patterned layers before annealing, for the high implantation density, the surface of the (001) wafer is free of defects due to the buried oxide, whereas line defects reach the surface of the (111) wafer. The data are consistent with the 27% greater stiffness and greater elastic anisotropy of the (111) plane of Si with respect to the (001) plane.[18] Si(001) substrates are therefore more suitable than Si(111) substrates for strain distribution control.

The volume of a given inclusion is approximately double its Si content prior to implantation. This volume expansion leads to a strain distribution in the substrate. For an elastically isotropic medium, the trace of the two-dimensional strain tensor evaluated in the surface plane is

$$\varepsilon(x,y)=\frac{C}{(x^2+y^2+L^2)^{3/2}}\left[\frac{3L^2}{(x^2+y^2+L^2)}-1\right], \qquad (1)$$

where x and y are orthogonal distances in the surface plane from the place directly above a point inclusion at a depth L. C is a constant. This equation was derived by Tersoff *et al.* from earlier work by Maradudin and Wallis.[12,19]

From investigations of samples from the six wafers described above, we were able to distill the following results. Figure 3 shows AFM images of a strain-distribution-controlled Si(001) wafer implanted at a density of 5×10^{16} cm^{-2}, measured in air in a clean room. Figure 3(a) shows a large scale (100 μm on a side) image of line patterns, demonstrating the wafer-scale nature of the process product. Figure 3(b) is a smaller scale image, which shows the behavior of steps in the vicinity of a 700-nm

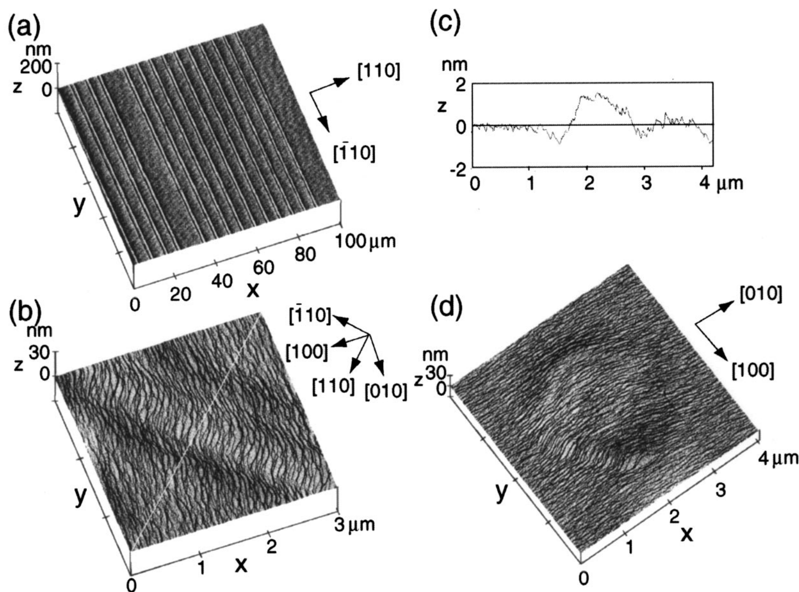

FIG. 3. (a) AFM image of line patterns, which vary in implanted width from 1.2 μm on the left to 400 nm on the right. [110] and $[1\bar{1}0]$ axes are parallel to the edges of this image. (b) AFM image of a 700-nm implantation width line pattern. (c) Topography from the bottom left to the top right along the white line in (b). (d) As (b) except for a 2-μm implantation diameter hole pattern. The data in (a), (b) and (d) are topographic, illuminated by a light source.

implantation-width line. It is noteworthy that the continuous step structure observed is that originally present at the Si(001)/oxide interface, where the oxide was removed by chemical etching. This step structure was obtained without ever inserting the sample in an ultrahigh vacuum. The details of the step structure formation are described in Ref. 20. Step bunching to a typical bunch height of about 0.5 nm is observed along the line pattern, which is qualitatively consistent with the theory of stress-induced step bunching on vicinal surfaces by Tersoff *et al.*[21] In addition, kink bunching occurs. The [110] and $[1\bar{1}0]$ kinks on the [100] oriented step kink bunch, ensuring that the step orientation as it crosses the line is approximately perpendicular to $[1\bar{1}0]$. Kink bunching is the plan-view analog of the step-bunching case considered in the cross section by Tersoff *et al.*[21]

Figure 3(c) shows the line topography in Fig. 3(b). The center of the line has risen by about 2 nm relative to the nonimplanted surface due to the volume expansion accompanying oxide inclusion growth. In Fig. 3(a), the 2-nm topographic scale is replicated over a square area 100 μm on a side.

To obtain a quantitative estimate of the maximum stress and strain present at the surface of the substrate, micro-Raman spectroscopy measurements were performed on a strained line after the 200-nm-thick Si buffer growth. The results are shown in Fig. 4. A substrate with the high implantation density was prepared by a procedure different from that in Fig. 1 in order to produce a surface topography with visible contrast in an optical microscope. Correcting for the 1-μm resolution and the difference in the preparation procedure, we estimate that the maximum stress at the center of the line pattern in Fig. 3(b) is 13 ± 3 MPa in each orthogonal surface direction. Using the two-dimensional elastic modulus of Si(001), 13 MPa corresponds to an in-plane tensile strain of approximately 0.007%.[22] It is remarkable that such a small value of strain produces the dot alignment effects observed in Figs. 5 and 6.

B. Self-assembly of Ge islands on the strained surfaces

Figures 5(a)–(c) show tapping mode AFM images of the surface after growth of Ge on the strain-distribution-controlled Si(001) surface as shown in Fig. 3. The Ge grows, forming three-dimensional islands surrounded by a wetting layer.[5,6] This growth mode occurs to reduce the combined surface energy and elastic energy of the system; the elastic energy arises due to the approximately 4% greater lattice constant of Ge with respect to Si.[20] Growth on a 700-nm implantation width line pattern produces straightly aligned, closely spaced islands with 140-nm mean diameter and 23-nm mean height, in a highly uniform size distribution [Fig. 5(a)]. Figures 5(d) and (e) are the size distributions of Ge dome islands on the implanted line and nonimplanted

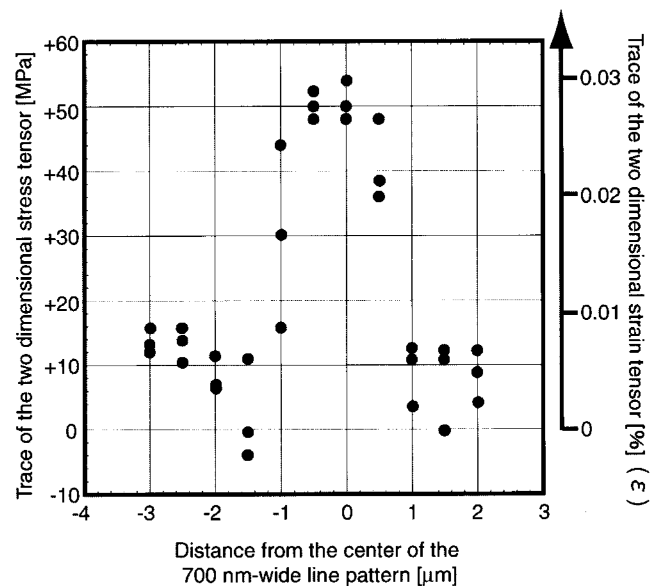

FIG. 4. Line scans of micro-Raman spectroscopy data at a wavelength of 457 nm. The surface was sampled at a depth of about 200 nm.

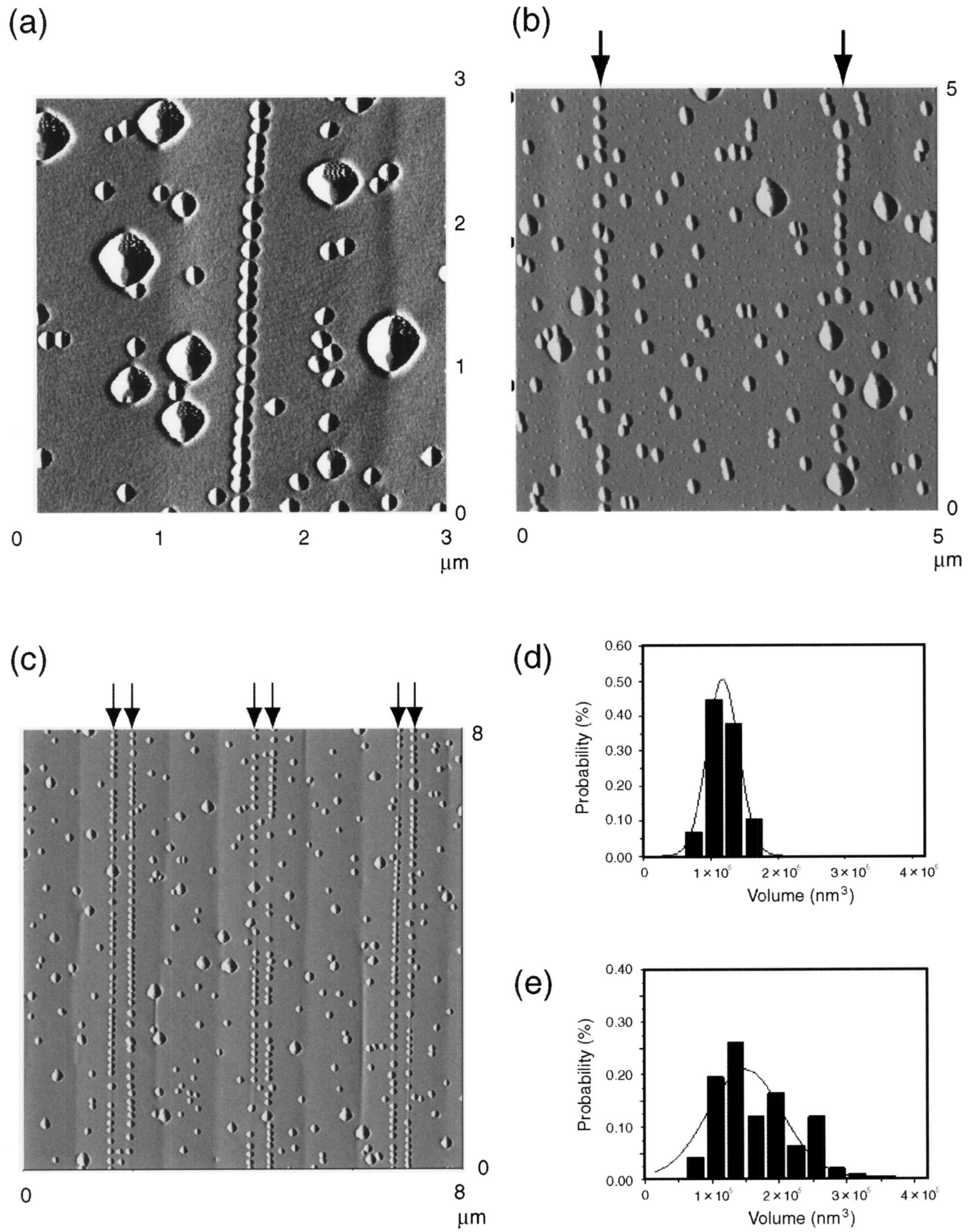

FIG. 5. (a) Gradient-mode AFM images of the surface after growth of Ge on a 700-nm implantation width line pattern. Size distribution of Ge dome shaped-islands on (d) the implanted region and (e) the nonimplanted region. Gradient-mode AFM images of the surface after growth of Ge on (b) a 4-μm and (c) 1.5-μm implantation width line patterns. The arrows indicate the positions of the two dot lines.

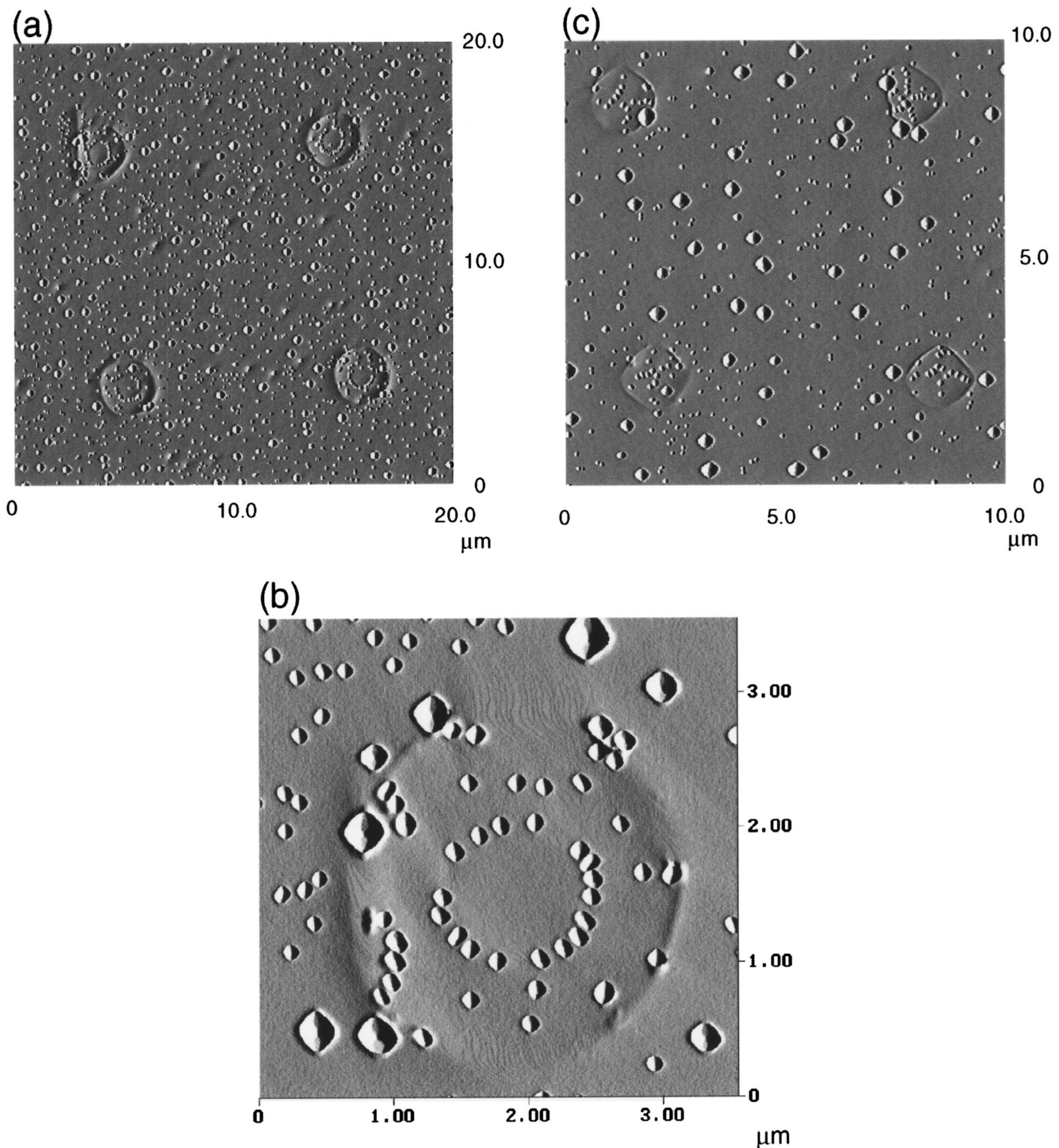

FIG. 6. Gradient-mode AFM images of the surface after growth of Ge on 2-μm (a) and (b), and 1.5-μm (c) implantation diameter hole patterns. [110] and $[1\bar{1}0]$ axes are parallel to the edges of the images.

regions. The standard deviations of diameter and height (7.8 and 2.2 nm, respectively) of these islands were reduced by a factor of 2 compared to the same type of island grown on the nonimplanted region [compare Figs. 5(d) and (e)]. In addition, only one island type (the "dome" type) grows on the line pattern—the reduction in the island size distribution is therefore greater still since a much larger island type (the "superdome") grows elsewhere.[6] The removal of Ge islands that grow at random on the nonimplanted regions is described at end of this subsection.

Growth on the wider implantation line produces two aligned straight lines of uniform Ge islands near the edges of the 4-μm implantation width line [Fig. 5(b)] and near the centers of the 1.5-μm implantation lines [Fig. 5(c)]. The distances between the two dot lines are about 2.8 and 0.4 μm. The alignment of the two lines of dots was confirmed for up to the 8-μm implantation width line. The distance between the two lines D (micrometers) was found to be proportional to the width of implantation line pattern W (micrometers) as $D=0.94W-1.0$ ($W>1.5$ μm). These results indicate that

the location and number of the lines can be exactly controlled by initial implantation line width.

It should be noted here that processed substrates (e.g., in Fig. 3) contain some defects. The pin-hole density is $\sim 10^5$ cm^{-2}. Dislocations are observed in places: They align parallel to and occur within the line patterns at a density of $\sim 10^6$ cm^{-2}. However, they have a negligible influence on dot alignment. Such dislocations can occur at any lateral position within a line pattern, but the dots are always aligned near the line pattern center. Consistent with Ref. 16, we expect substantial reductions in the defect density with future development.

Figures 6(a)–(c) are AFM images of hole patterns with 2-μm [(a) and (b)] and 1.5-μm (c) diameters after the 7.5-ML-thick Ge island growth. The islands have self-organized into a ring at the center of all implanted hole patterns 2 μm in diameter [Figs. 6(a) and (b)]. No dot rings were obtained for hole patterns 1.5 μm [Fig. 6(c)] to 700 nm in diameter. It should be noted, however, that the density of the islands on the implanted regions without dot rings is larger than that on the nonimplanted regions, suggesting that the implanted regions are under tensile strain.

Further experiments on Ge island growth showed that the Ge islands on the implanted regions change shape similarly to the manner in which they do on nonimplanted regions: the shape changes from hutlike, to pyramidlike, to domelike, and finally to superdomelike with increasing Ge coverages.[23] Imperfections in the line and hole pattern island arrangements are most probably due to nonideal oxide inclusion distribution in the bulk.

In addition, we could not observe clear alignment of Ge islands on the line implanted regions for 1×10^{16}- and 3×10^{16}-cm^{-2} O ion doses. This indicates that those doses do not produce sufficient stress on the Si(001) surface for Ge island alignment.

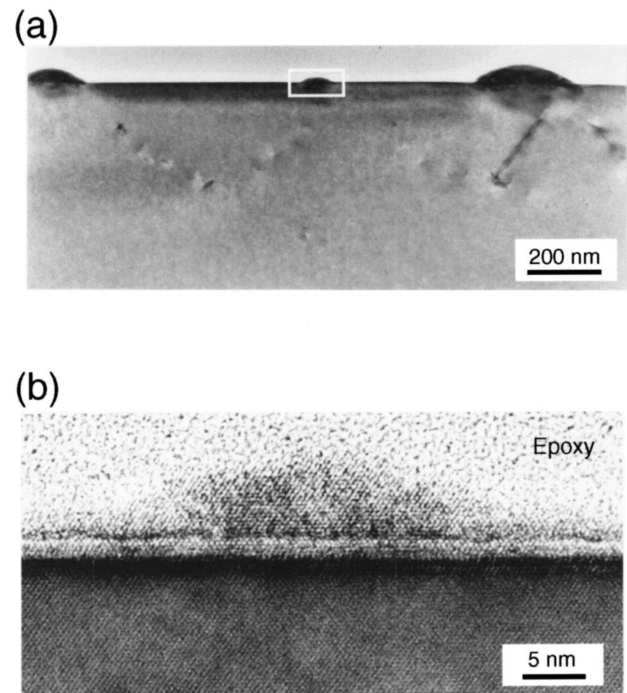

FIG. 7. (110) cross-sectional TEM images of line patterns perpendicular to (110). (a) 700-nm implantation width line pattern on which Ge was grown. (b) Lattice resolution image of area enclosed in the white box in (a).

Figure 7 shows cross-sectional TEM images obtained from a strain-distribution-controlled Si(001) substrate line pattern after Ge island growth. As shown in Fig. 5(a), the Ge islands have a domelike shape and are aligned on the line. Figure 7(a) shows a Ge dome that has grown at the center of the line pattern (white box). Figure 7(b) shows a lattice-resolution image of the Ge dome in Fig. 7(a), including the wetting layer. The growth is coherent. Also, no defects are visible in the substrate. These TEM observations indicate that the Ge island alignment is caused by the strain distribution on the surface produced by buried oxides, not by lines originating from dislocations. This is consistent with the following simulations.

Simulations of the strain distribution at the substrate surface were performed in order to understand the narrow lateral spread of island positions in Fig. 5(a), the two lines of aligned Ge islands in Fig. 5(c), the dot ring shape in Fig. 6(a), and the absence of the dot ring shape in Fig. 6(c). No fitting parameters were used. The results for idealized distributions of bulk inclusions are shown in Fig. 8, where (a) and (b) confirm that the spread in the island lateral positions for the 700-nm implantation width line pattern should be small, (c) and (d) confirm that two aligned lines of dots should be produced on the 3-μm implantation width line in Fig. 5(c), and (e) and (f) verify that a ring shape of dots should be produced, as observed in Fig. 6(a). The predicted diameter of the ring is 1.25 μm, which is very similar to the 1.1 ± 0.1-μm diameter observed. The most likely explanation for the small difference is that the inclusion distribution differs from the idealized one. For example, simulations for inclusions confined to a disc 1.8 μm in diameter predict a dot circle diameter of 1.05 μm, which is in better agreement with experiment. Simulations of hole patterns 1.5 μm to 700 nm in diameter predict no circle of dots within the inclusion uniformity implied by the gaps in the dot rings in Fig. 6(a) [see Figs. 8(g) and (h)]. This is in agreement with experiment: dot rings were not obtained for hole patterns 1.5 μm to 700 nm in diameter [Fig. 6(c)]. For accurate strain distribution prediction, we emphasize the importance of using a two-dimensional strain function, as in Eq. (1), rather than the one-dimensional strain function used by Tersoff *et al.*[12] Note, however, that the simulation of the 1.5-μm implantation width line does not produce two clear maxima of tensile strain across the line (not shown here) in contrast to Figs. 8(c) and (d). This is not in agreement with the experimental result in Fig. 5(c). This discrepancy might be overcome by taking into consideration the elastic interactions between the Ge islands through the strained silicon substrate in the elastic simulation, or it could be due to an oxide inclusion distribution which differs from that idealized.

Next, in addition to the creation of the tensile strained regions for Ge island localization control, we show how to create a compressive strained region on a Si wafer. Figure 9(a) shows an AFM image of a surface after growth of Ge

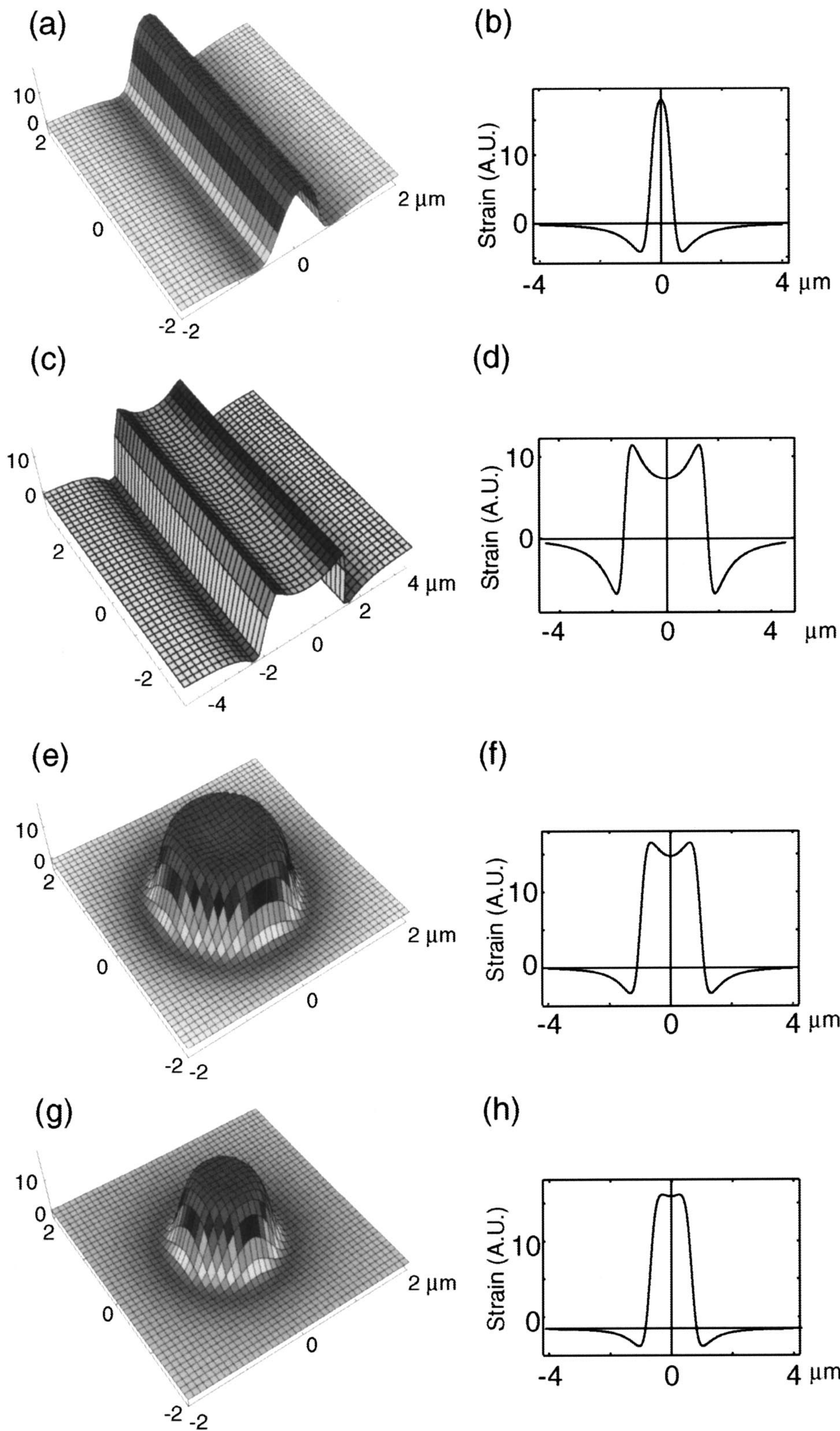

FIG. 8. Plots of the total strain function evaluated at the surface using Eq. (1), for a square lattice of inclusions in which the inclusions are 100 nm apart and 300 nm below the surface. The horizontal axes correspond to surface distances in micrometers; the vertical scales are in dimensionless units CL^{-3}. (a) The array is 600 nm wide by 10 μm long. The central 4×4-μm area is shown. (b) Cross section perpendicular to the center of the line pattern in (a). (c) The array is 4 μm wide by 10 μm long. The central 8×4-μm area is shown. (d) Cross section perpendicular to the center of the line pattern in (c). (e) The array is confined to a disc 2.0 μm in diameter. (f) The cross section of (e). (g) The array is confined to a disc 1.4 μm in diameter. (h) The cross section of (g).

islands on arrays of 700-nm implantation width lines with 1-μm-wide spaces between the lines. The corresponding simulation is shown in Fig. 9(b). As seen in this figure, compressive strained regions emerged in the region between the implantation lines [see region C in Fig. 9(b)]. The emergence of these regions is supported by the fact that lines of dots formed on the implantation lines as shown in the simulation on tensile regions [Fig. 5(a)]. Therefore we can say from the simulation that compressive regions on a micrometer scale were produced by long-range elastic interactions between the

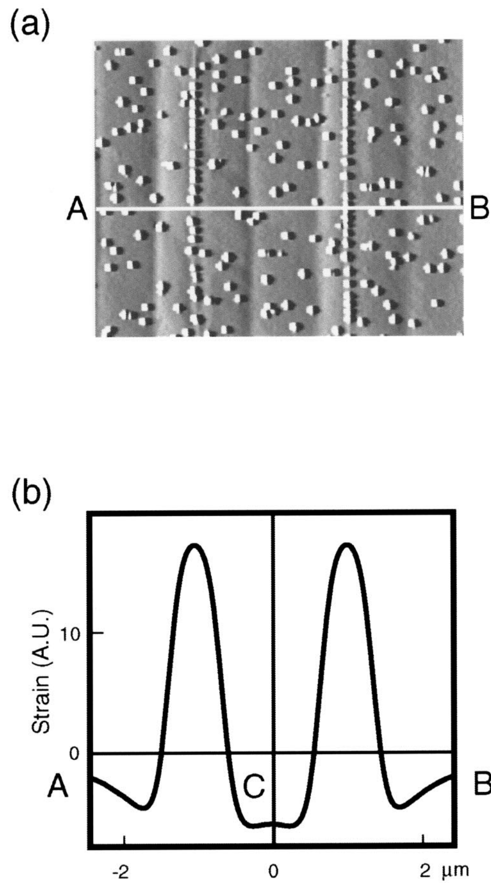

FIG. 9. (a) Gradient-mode AFM images of the surface after growth of Ge on arrays of 700-nm implantation width lines with 1-μm nonimplantation width line spaces. One line of self-assembled uniform Ge dots is visible on each implantation line. The image size is 5×4 μm. (b) Cross section of the total strain of the line arrays along the white line A-B in (a), evaluated as in Fig. 8. The lines are 700 nm wide by 10 μm long.

tensile strained regions and the use of the interaction is one way to form regions of localized compressive strain on a Si wafer. We could not, however, find any characteristic feature of the compressive strain effect on the Ge island growth in Fig. 9(a), although we see that the localized compressive and tensile stresses in Fig. 8 clearly affect the stability of steps. The steps on the strained regions are bunched and curved due to the localized strains as seen in Figs. 3(b) and (d).

Finally, we discuss how to remove the large number of randomly positioned dots on the nonstrained regions, which is necessary because these dots would degrade the functions of future nanodot devices. To solve this problem, we changed the Ge island growth temperature from 550 to 600 °C. The 50 °C increase significantly reduced the density of stray dots on nonstrained regions, and thus resulted in the localization of big and dislocated Ge islands only on strained line and hole regions, as seen in Figs. 10(a) and (b). This indicates that the increase in the growth temperature made the diffusion length of Ge atoms on the Si surface long enough for the Ge atoms to find the more energetically suitable sites for nucleation and growth.[11,12,24] Therefore if we can optimize

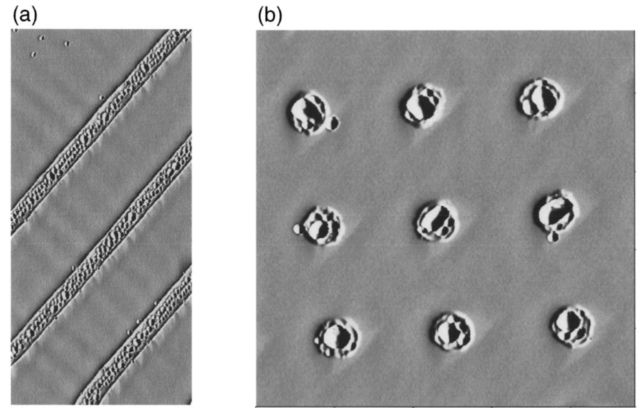

FIG. 10. Gradient-mode AFM images of the surface after growth of Ge on 1-μm implantation width lines with 5 μm wide line spaces (a) and 1-μm diameter hole patterns that were located with a period of 4 μm. The image sizes are 12×25 μm for (a) and 12×12 μm for (b).

the Ge growth conditions for the local strain distribution we initially designed on a Si wafer, we should be able to align uniform self-assembled and dislocation-free Ge dots on the artificially designed regions on the Si wafer without having stray dots grow randomly on nonstrained regions.

IV. CONCLUSION

We have proposed and demonstrated a different way to control the strain distribution on Si(001) and Si(111) surfaces on a wafer scale and shown that this can be applied for the control of nanoscale Ge island self-assembly on the Si(001) surface. The approach applies commercially viable, industrially proven processes to prepare the Si wafer for nanostructure fabrication. We expect that this strain distribution control method will be readily extended to shorter length scales in future work. Shorter scales than those reported here can be achieved in optical lithography, and lower energy implantation will reduce the depth of the oxide inclusions.

The technique used here, a combination of ion implantation and annealing that leads to a strain distribution suitable for nanofabrication control, is not restricted to the Ge-on-Si system: We hope that our results will inspire researchers in other fields to try out the same basic approach, especially since our results demonstrate a different fabrication control technique in the highly topical field of nanofabrication. Furthermore, we hope that this work will open up a new chapter in the field of surface science, particularly the physics on a surface under localized stress and strain, and inspire surface scientists.

ACKNOWLEDGMENTS

This work was supported by the NEDO International Joint Research Grant Program. The authors thank Rosei for some AFM measurements, not included here, H. Sugiyama for TEM measurements, and H. Ando for coordinating micro-Raman observations. They also thank Dr. H. Yamaguchi for useful comments.

*Author to whom correspondence should be addressed. Email address: homi@will.brl.ntt.co.jp

†Present address: 15 Crown Lane, Benson, Wallingford OX10 6LP, United Kingdom.

‡Present address: Division of Architecture and Building Science, Yokohama National University, Yokohama, Japan.

[1] The International Technology Roadmap for Semiconductors, 2001 (http://public.itrs.net/Files/2001ITRS/Home.htm).

[2] T.-C. Shen, C. Wang, J. W. Lyding, and J. R. Tucker, Appl. Phys. Lett. **66**, 976 (1995).

[3] F. Liu and M. G. Lagally, Surf. Sci. **386**, 169 (1997).

[4] D. J. Eaglesham and M. Cerullo, Phys. Rev. Lett. **64**, 1943 (1990).

[5] F. M. Ross, R. M. Tromp, and M. C. Reuter, Science **286**, 1931 (1999).

[6] G. Medeiros-Ribeiro, A. M. Bratkovski, T. I. Kamins, D. A. A. Ohlberg, and R. S. Williams, Science **279**, 7353 (1998).

[7] H. Omi and T. Ogino, Phys. Rev. B **59**, 7521 (1999).

[8] O. G. Schmidt, N. Y. Jin-Phillipp, C. Lange, U. Denker, K. Eberl, R. Schreiner, H. Gräbeldinger, and H. Schweizer, Appl. Phys. Lett. **77**, 4139 (2000).

[9] T. I. Kamins and R. S. Williams, Appl. Phys. Lett. **71**, 1201 (1997).

[10] G. Jin, J. L. Liu, and K. L. Wang, Appl. Phys. Lett. **76**, 3591 (2000).

[11] C. Teichert, M. G. Lagally, L. J. Peticolas, J. C. Bean, and J. Tersoff, Phys. Rev. B **53**, 16 334 (1996).

[12] J. Tersoff, C. Teichert, and M. G. Lagally, Phys. Rev. Lett. **76**, 1675 (1996).

[13] H. Omi, D. J. Bottomley, and T. Ogino, Appl. Phys. Lett. **80**, 1073 (2002).

[14] H. Omi, D. J. Bottomley, Y. Homma, T. Ogino, S. Stoyanov, and V. Tonchev, Phys. Rev. B **66**, 085303 (2002).

[15] K. Izumi, M. Doken, and H. Ariyoshi, Electron. Lett. **14**, 593 (1978).

[16] J.-P. Colinge and R. W. Bower, MRS Bull. **23**, 13 (1998).

[17] R. F. Service, Science **281**, 893 (1998).

[18] D. J. Bottomley and P. Fons, J. Cryst. Growth **160**, 406 (1996).

[19] A. A. Maradudin and R. F. Wallis, Surf. Sci. **91**, 423 (1980).

[20] D. J. Bottomley, H. Omi, Y. Kobayashi, M. Uematsu, H. Kageshima, and T. Ogino, Phys. Rev. B **66**, 035301 (2002).

[21] J. Tersoff, Y. H. Phang, Z. Zhang, and M. G. Lagally, Phys. Rev. Lett. **75**, 2730 (1995).

[22] J. Hornstra and W. J. Bartels, J. Cryst. Growth **44**, 513 (1978).

[23] I. Daruka, J. Tersoff, and A.-L. Barabási, Phys. Rev. Lett. **82**, 2753 (1999).

[24] Q. Xie, A. Mudhukar, P. Chen, and N. P. Kobayashi, Phys. Rev. Lett. **75**, 2542 (1995).